



<b>Publication Year</b>	2022
<b>Acceptance in OA @INAF</b>	2023-05-22T12:36:43Z
<b>Title</b>	Key wavefront sensors features for laser-assisted tomographic adaptive optics systems on the Extremely Large Telescope
<b>Authors</b>	Thierry Fusco; AGAPITO, Guido; Benoit Neichel; Sylvain Oberti; Carlos Correia; et al.
<b>DOI</b>	10.1117/1.JATIS.8.2.021514
<b>Handle</b>	<a href="http://hdl.handle.net/20.500.12386/34176">http://hdl.handle.net/20.500.12386/34176</a>
<b>Journal</b>	JOURNAL OF ASTRONOMICAL TELESCOPES, INSTRUMENTS, AND SYSTEMS
<b>Number</b>	8

# Key wavefront sensors features for laser-assisted tomographic adaptive optics systems on the Extremely Large Telescope

Thierry Fusco<sup>a,b,\*</sup>, Guido Agapito<sup>c,\*</sup>, Benoit Neichel,<sup>b</sup>  
Sylvain Oberti,<sup>d</sup> Carlos Correia<sup>b</sup>, Pierre Haguenaer,<sup>d</sup> Cédric Plantet<sup>b,c</sup>,  
Felipe Pedreros<sup>b</sup>, Zibo Ke,<sup>b</sup> Anne Costille,<sup>b</sup> Pierre Jouve,<sup>b</sup>  
Lorenzo Busoni<sup>b,c</sup> and Simone Esposito<sup>c</sup>

<sup>a</sup>Université Paris Saclay (COMUE), DOTA, ONERA, Châtillon, France

<sup>b</sup>Aix Marseille University, CNRS, CNES, LAM, Marseille, France

<sup>c</sup>INAF, Arcetri Astrophysical Observatory, Firenze, Italy

<sup>d</sup>European Southern Observatory, München, Germany

**Abstract.** Laser guide star (LGS) wave-front sensing (LGSWFS) is a key element of tomographic adaptive optics system. However, when considering Extremely Large Telescope (ELT) scales, the LGS spot elongation becomes so large that it challenges the standard recipes to design LGSWFS. For classical Shack–Hartmann wave-front sensor (SHWFS), which is the current baseline for all ELT LGS-assisted instruments, a trade-off between the pupil spatial sampling [number of sub-apertures (SAs)], the SA field-of-view (FoV) and the pixel sampling within each SA is required. For ELT scales, this trade-off is also driven by strong technical constraints, especially concerning the available detectors and in particular their number of pixels. For SHWFS, a larger field of view per SA allows mitigating the LGS spot truncation, which represents a severe loss of performance due to measurement biases. For a given number of available detectors pixels, the SA FoV is competing with the proper sampling of the LGS spots, and/or the total number of SAs. We proposed a sensitivity analysis, and we explore how these parameters impacts the final performance. In particular, we introduce the concept of super resolution, which allows one to reduce the pupil sampling per WFS and opens an opportunity to propose potential LGSWFS designs providing the best performance for ELT scales. © The Authors. Published by SPIE under a Creative Commons Attribution 4.0 International License. Distribution or reproduction of this work in whole or in part requires full attribution of the original publication, including its DOI. [DOI: [10.1117/1.JATIS.8.2.021514](https://doi.org/10.1117/1.JATIS.8.2.021514)]

**Keywords:** adaptive optics; wavefront sensors; tomography; lasers; telescopes.

Paper 21174SS received Dec. 20, 2021; accepted for publication Jun. 3, 2022; published online Jun. 20, 2022.

## 1 Introduction

Europe has just launched the construction of the largest ground-based telescope: the Extremely Large Telescope (ELT).<sup>1</sup> In operation by 2027, this 40-m giant will answer fundamental questions from the search for and characterization of planets to the formation and evolution of the first galaxies of the universe. Adaptive optics (AO), by correcting in real-time aberrations introduced by the atmosphere, is essential to reach the ultimate performance of this future facility. The ELT has therefore been designed as an adaptive telescope, which will provide images with an angular resolution of <10 milliarc second in the near infrared. For this purpose, the ELT is equipped with a deformable mirror in its optical train (the fourth mirror of the telescope, alias ELT M4<sup>2</sup>), as well as six to eight laser stations,<sup>1</sup> to create artificial sources [laser guide stars (LGS)] for wavefront analysis. Laser stars have been used in AO on 8/10-m telescopes for about 20 years now, and their performance is relatively well mastered. However, scaling up to a 40-m telescope represents

\*Address all correspondence to Thierry Fusco, [thierry.fusco@onera.fr](mailto:thierry.fusco@onera.fr); Guido Agapito, [guido.agapito@inaf.it](mailto:guido.agapito@inaf.it)

†Co-first authors

a much bigger challenge than a simple extrapolation of the current solutions, and new concepts are required, especially in the field of wavefront sensing.

In this work, we focus on Shack–Hartmann wave-front sensing (SHWFS) because it is currently the best suited WFS for LGSWFS. Although alternative solutions, such as Pyramid<sup>3</sup> and Ingot WFS,<sup>4</sup> exist and are pursued actively,<sup>5,6</sup> they still have to be proved on the sky and are therefore deemed not mature enough to be used within the ELT. Despite being a forced choice for LGS sensing, the SHWFS in the context of ELT has a major downside as it requires a detector with a large number of pixels to satisfy at the same time the requirement on the extended spot sampling, both in term of pixel pitch and overall FOV, and on turbulence spatial sampling.<sup>7–9</sup>

Although our work is general, it is particularly interesting for the tomographic AO systems of a couple of first light instruments of the ELT: multi-conjugate AO RelaY (MAORY)<sup>10</sup> and High Angular Resolution Monolithic Optical and Near-infrared Integral field spectrograph (HARMONI).<sup>11</sup> We report in the following sections several examples derived from these instruments and the LGSWFS main parameters that we propose can be directly applied to them.

In this paper, we present the challenges of Laser-assisted tomography on ELT (Section 2), and the impact on the design of LGSWFS. Section 3 deals with a new concept, dubbed super-resolution, which allows one to obtain good tomographic performance, with a reduced number of pupil sampling points. Sections 4 and 5 deal with the specific application to the ELT case, in particular we analyse the impact of the sub-aperture (SA) size, of the spot sampling and truncation and of the noise propagation on the AO system performance. Finally, in Section 6, we report potential LGSWFS designs considering the performance sensitivities presented in the previous sections.

## 2 Challenges of Laser-Assisted Tomographic AO on the ELT

This section summarizes the main challenges imposed by the use of LGS for an ELT.

### 2.1 Tip–Tilt Information

This is a well known problem for AO systems working with LGSs: the image motion (or tip–tilt modes) cannot be measured directly from the LGS itself.<sup>12</sup> The transition from 8 to 40 m does not significantly change this fundamental limitation, and the LGS AO systems still require the use of a natural guide star (NGS) to get these modes. Fortunately, we have some favorable factors for the determination of tip–tilt in the detection of wavefront error: (1) the isoplanatic angle of low-order modes like tip–tilt is an order of magnitude larger than that of high-order modes. And for an ELT, the outer scale of the turbulence can play a positive role in reducing the overall atmospheric tip–tilt energy. (2) The entire pupil of telescope can be used to measure the tip–tilt, and as a result, the NGS used for measuring tip–tilt only can be significantly fainter than the usual NGS stars in classical AO. A full ELT pupil should allow access to fainter stars than an 8-m telescope, hence potentially increasing the sky coverage. (3) The temporal bandwidth of the close loop in terms of tip–tilt compensation is about 1/4 of that of the high order (the Zernike polynomial cutoff frequency scales linearly with the radial degree as can be seen in Ref. 13), which can be beneficial for increasing the integration time, hence improving the SNR on faint NGS. On the downside, one has to note that this is true for atmospheric tilt, but telescope vibrations or wind-shake, which becomes much stronger for an ELT, would still require a large temporal bandwidth for measurement and control. Note that the NGS performance estimation is provided in a companion paper (Plantet,<sup>14</sup> Neichel et al. this review).

### 2.2 Cone Effect

The second main limitation of the LGS is the cone effect.<sup>15</sup> The laser is focused at finite altitude [somewhere in the middle of the sodium (Na) layer], hence, the wave we receive from the laser source is spherical. If an AO system can only use a single LGS beacon to sense the atmospheric turbulence, an error is made; this error is called cone effect or Focus Anisoplanatism. The larger the diameter of the telescope, the more important the cone effect becomes. The mitigation to

cone effect is to use more than a single LGS and perform a tomographic reconstruction of the atmospheric volume above the telescope. This is further detailed in Sec. 3.

### 2.3 Spot Elongation

The spot elongation comes from the fact that the laser stars are not point objects but extended sources. Indeed, the layer of Na atoms, located at 90 km above the telescope, has a thickness between 10 and 20 km. The laser stars resulting from the excitation of these Na atoms by the laser light propagated from the telescope have thus a cigar shape in the Na layer. By perspective effect, they appear as extended objects (approximately like ellipses) on the opposite edge of the telescope pupil. For a 40-m telescope, the laser spots have a size between 1 arcsecond for those close to the Laser Launch Telescope (LLT) and a maximum expected elongation, which can reach up to 25 arc sec. The difficulty is therefore to perform a wave front analysis on highly extended objects, and whose elongation varies in the pupil. There has been several options proposed in the literature to mitigate the spot elongation issue. The proposed solutions include modifications of the laser source itself,<sup>16</sup> innovative WFS strategy,<sup>17</sup> and advanced centroiding algorithms.<sup>18</sup> Of course these solutions are not exclusive, and a combination of some is possible.

The mitigation followed in this work is based on the work developed by Béchet et al.<sup>19</sup> The method consists in weighting the measurements in order to only reject the ones along the long axis of the elongation (truncated) while keeping those along the small axis (not truncated). For each spot, the gradient along the small axis would be kept, whereas the gradient along the long axis would be rejected if truncated. Due to the redundancy of the measurements, and the fact that in a side-launch configuration the elongated spots of one WFS correspond to the non-elongated spots of another WFS, the expected impact on performance should be small. This is detailed in Sec. 4.

The above-mentioned topic of LGS spot truncation naturally leads to a necessary trade-off between the LGS spot sampling and the total field-of-view (FoV), in the context of the technological limitation imposed by current state of detectors. In fact, for a fixed number of pixels associated with an SHWFS, and a fixed number of SAs, a potential solution to increase the FoV of each SA could be to increase the angular size of each pixel. Usually, the SHWFSs are designed to have a pixel size providing the Shannon sampling of the spots within each SA [when not photon or read-out noise (RON) limited]. For the LGS object, the smaller spot size that one can expect may be around 1 arc sec FWHM. In this case, the ideal pixel size should be 0.5 arc sec. Fixing the pixel size, if the detector and number of subapertures are fixed, will automatically determine the FoV of the WFS. Increasing the pixel size can then be an option to increase the subaperture FoV and mitigate LGS truncation. However, working with larger pixels introduces an undersampling of the LGS spot, which induces non-linear effects (optical gains) in the centroid measurement.<sup>20–22</sup> The extreme example would be working with quad-cells ( $2 \times 2$  pixels per subaperture), which are known to be very non-linear.<sup>23</sup> Basically, when working with under-sampled spots, the centroiding will become a function of the LGS spot size. For LGSWFS, and because the spot size changes across the pupil, the non-linearity will be different for each SA, making the wave-front reconstruction very complex. This dependence (known as optical gain for the pyramid WFS) has to be calibrated on-line, e.g., by dithering each LGS with a known signal.<sup>24</sup> Even though this on-line calibration is feasible, it adds complexity to the AO system, and centroid gains remain an additional error in the final performance of multi-LGS systems.<sup>25</sup> This trade-off has been a key topic in the design and definition of the LGSWFSs for the ELT.

### 2.4 Key Parameters for Laser WFSensing on the ELT

As said above, several parameters will be impacting the final performance of the laser assisted AO system for the ELT. In the following, we explore the performance sensitivity to several of these parameters. In particular, we investigate the following aspects:

1. Pupil sampling (a.k.a. number of SAs) and tomographic performance.
2. LGS spot sampling versus truncation trade-off.
3. Noise propagation (flux and RON).

It is worth noting that in this work we aim at minimizing the sum of all the error terms (fitting, aliasing, noise, linearity, and truncation) given the constraints of the available technology in terms of detectors. As we will show in the following sections, this brings the design in the direction of sub-optimal choice with respect to single issues like linearity and truncation. In fact, we could design WFSs that completely avoid these last two error terms, but at the price of a lower overall performance. In the same way, using a large number of pixels per SA makes the noise larger, but it is the best overall solution to balance linearity and truncation errors.

Finally, note that in this work, we do not focus on temporal error because the WFS characteristics we are interested in have no impact on it and, moreover, its weight in the overall error budget for first generation tomographic AO systems on the ELT is negligible with respect to the other terms presented here. In fact, it can be easily shown<sup>26</sup> that for the median atmospheric condition of Cerro Armazones<sup>27</sup> we expect a temporal error of about 50 nm for a closed loop framerate of 500 Hz, much smaller than the error budget of HARMONI and MAORY (see Refs. 14 and 28, Neichel et al. this review).

### 3 Tomography and Super-Resolution

Before detailing the optimization of the LGSWFS design for the ELT, we first introduce the concept of super-resolution,<sup>29,30</sup> and its application for tomographic AO systems.

On wide-field AO systems [either multi-conjugate AO (MCAO) or laser tomography AO (LTAO)], several WFSs sense the turbulence volume to get a tomographic information of the disturbances above the telescope. This tomographic information can then be used to optimize the performance in a given direction (single DM  $\rightarrow$  LTAO) or across a wider science FOV (several DM  $\rightarrow$  MCAO). This configuration gives also an additional feature: the different lines of sight of the WFSs increase the number of measurements in the part of the metapupil illuminated by more than one laser beam. As such, information at a higher spatial frequency than the Nyquist's one given by the number of SAs of a single WFS is accessible.<sup>31,32</sup> A few examples of the metapupil sampling of a tomographic system are shown in Fig. 1.

In other words, with multi LGS tomographic AO system without any intentional misalignment, the geometrical resolution is coming for free, at least for the turbulent layers in altitude. Unfortunately, this free super-resolution is effective in a reduced altitude range because at ground level all WFSs see the pupil with the same geometry and at high altitudes the sensed patch of the WFS separates between each other. In particular, the optimal shift of half SA is given at an altitude  $h_{\min}$  considering opposite LGSs and neglecting cone effect:

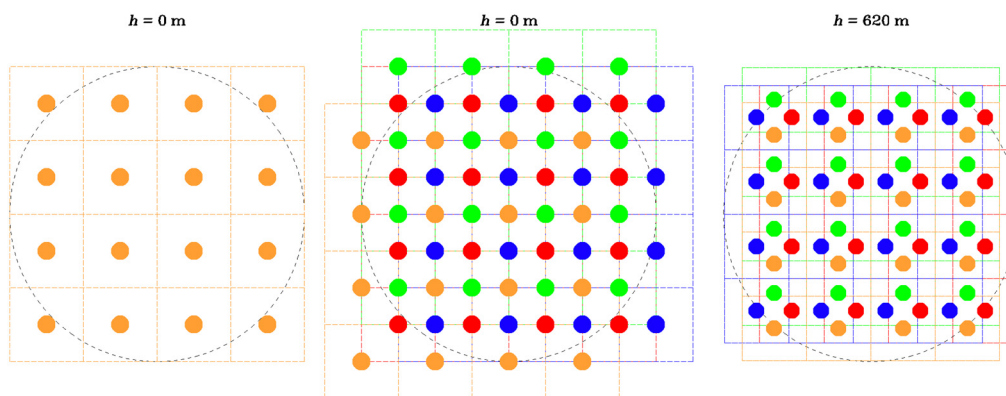


**Fig. 1** Example of meta-pupil sampling with four  $4 \times 4$  LGS WFSs with 50-cm SAs and an off-axis angle of 45 arc sec. Different colors are used to distinguish between the four WFSs. Left, altitude is 0 m and no super-resolution is present because all SAs are superimposed. Center, altitude is 0 m, and on purpose mis-alignments give a resolution of half the SA size. Right, altitude is 620 m, the same of ELT M4, and the SA shift coming from the four different lines of sight,  $\alpha = 45$  arcsec, give a naturally induced super-resolution that is approximately half the SA size.

$$h_{\min} = \frac{d}{4\alpha}, \quad (1)$$

where  $d$  is the size of an SA and  $\alpha$  is the LGS asterism radius. For MAORY,  $\alpha = 45$  arcsec, and HARMONI,  $\alpha = 34$  arcsec, considering an SA size of 50 cm, this value is 573 and 737 m, respectively, close to ELT M4 conjugation altitude (620 m). On the other hand, the altitude at which opposite LGS patch separates at zenith,  $h_{\max}$ , is

$$h_{\max} = \frac{Dh_{\text{Na}}}{D + 2\alpha h_{\text{Na}}}, \quad (2)$$

where  $D$  is the telescope diameter and  $h_{\text{Na}}$  is the average Na altitude. This value is 45 and 50 km for MAORY and HARMONI, respectively ( $h_{\text{Na}} = 90$  km). This means that a significant part of the turbulence volume is sensed at a higher resolution than the one given by the SA size, as can be seen in the example of Fig. 2. In this figure, the geometry of MAORY LGS asterism and the naturally induced relative shift between couple of WFSs is shown: only at 0 km, the relative shifts of all the couples of WFS is null, confirming our previous statement (note that this is true also for HARMONI).

Still, the lower part of the ground layer sensing (a few hundreds of m for MAORY and HARMONI) is limited by the SA size, unless misalignments between WFSs SA grids and pupil is voluntarily introduced. This is the strategy followed and is referred to as geometrical super resolution (GSR).

An example of Super Resolution is shown in Fig. 3, where the eigen value of the interaction matrix of a system composed by a  $41 \times 41$  actuator deformable mirror (DM) conjugated to the pupil and 4 WFS have been plotted for various cases:

1. A “classical case” for which the four WFSs are aligned and see the DM exactly in the same way (it corresponds to a classical single WFS system but we keep the four WFSs in order to keep the same number of measurements and normalization for all the cases). It corresponds to the dashed lines in Fig. 3.
2. A GSR case for which each WFS is shifted by half an SA in  $x$  and  $y$ . It corresponds to the solid lines in Fig. 3.

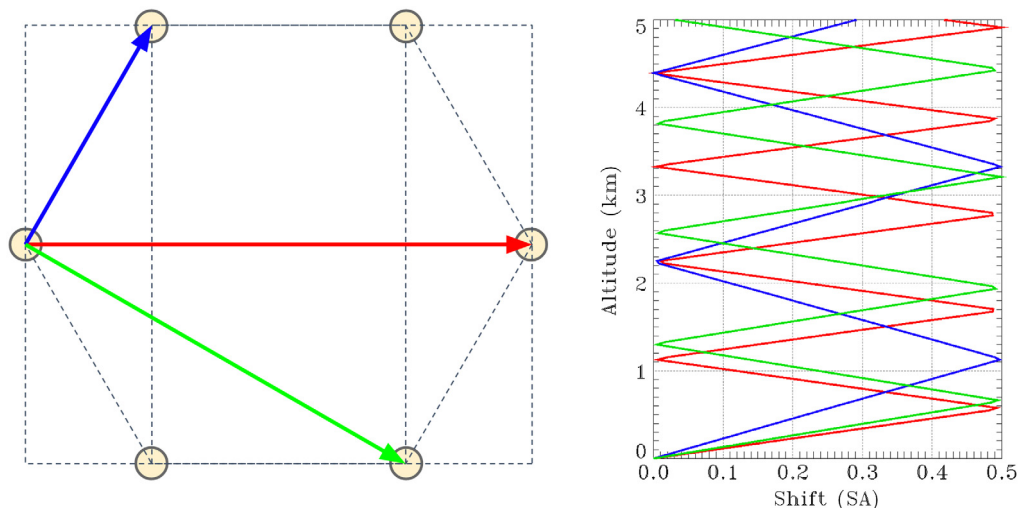


**Fig. 2** MAORY LGS asterism and the naturally induced relative shift as a function of the altitude (in the range 0 to 5 km) for three couples of WFSs (we used the same colors on the left and right parts of the figure). Sub-aperture (SA in the caption) size is 0.5 m and the value reported in the right part of the figure is the results of the modulo 1 operation and values  $>0.5$  are reported as the difference between 1 and the shift value. Where the shift is close to 0.5 SA the naturally induced super-resolution has the maximum effect, and it is completely not effective only when the shifts for all the couples of WFS is 0 (in this range only at an altitude of 0 km).

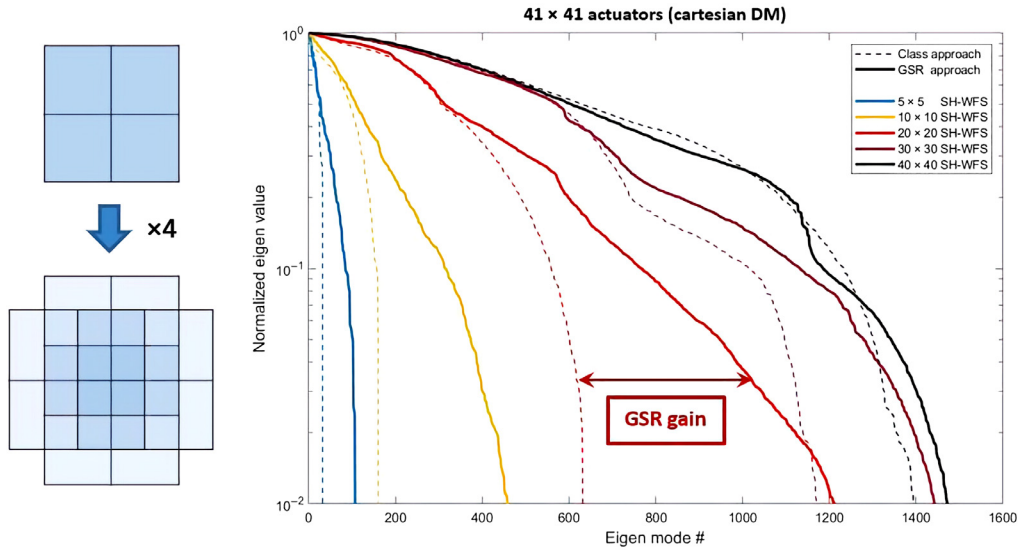
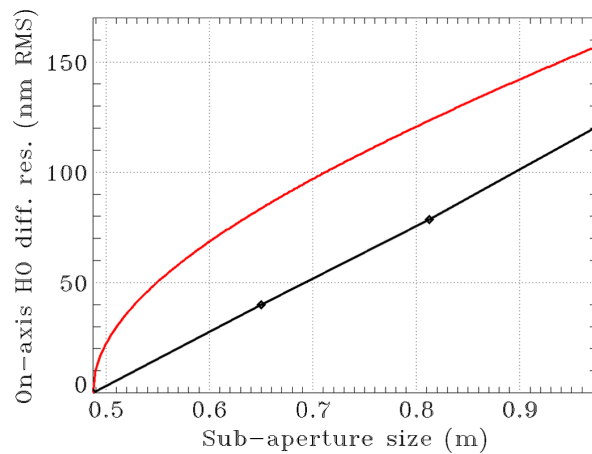


**Fig. 3** Impact on eigen values of the GSR with respect of the classical case for configuration with different numbers of SAs. A  $41 \times 41$  actuator DM is considered here. On the left the effect of GSR for a WFS with  $2 \times 2$  SA is shown.

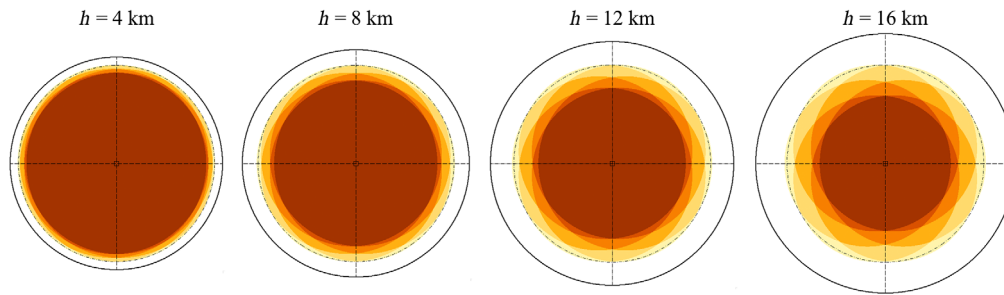
For both the classical and the GSR cases, we consider a WFS with a various number of SAs (from  $5 \times 5$  to  $40 \times 40$ , corresponding to various colors in Fig. 3) knowing that the reconstruction basis remains the same (the  $41 \times 41$  DM actuator basis for all the cases).

Figure 3 clearly shows the gain brought by the GSR when compared to a classical approach, in terms of number of accessible modes. In particular, it is shown that we have access to typically the same number of modes with a  $30 \times 30$  WFS with GSR as with a  $40 \times 40$  with a classical approach. Even though the eigen values are slightly lower for  $30 \times 30$  with GSR than  $40 \times 40$  with classical approach, the quadratic sum of the eigen value only shows a 15% decrease and therefore should not bring any significant degradation in terms of noise propagation.

The application of naturally induced super-resolution for MAORY (that means without any intentional misalignment) is shown in Fig. 4. Here, it is interesting to note that the expected error increase given by fitting error, shown in red, is following the law  $k_f \sqrt{d^{5/3} - d_0^{5/3}}$ , whereas the one found for super-resolution is following the law  $k_s(d - d_0)$ , where  $k_f = 194$ ,  $k_s = 248$  and



**Fig. 4** On-axis MAORY High Order (excluding tilts) differential (with respect to an SA size of 0.4875 m) residual as a function of SA size. High flux, no elongation. Red line, theoretical residual considering fitting error increase due to lower sampling. Black line is lower thanks to naturally induced super-resolution (that means without any intentional misalignment).



**Fig. 5** LGS beams overlap at different altitudes for MAORY working at a zenith angle of 30 deg. Decreasing color luminance is used to show an increasing number of overlapping beams. Dotted circles correspond to the pupil size, 39 m, and white portion corresponds to the area where the FoV is not sensed and it mainly corresponds to technical FoV.

$d_0 = 0.4875$ . We verified that all the tested configurations are able to properly correct the turbulence with all degrees of freedom of ELT M4, so the error reported above is not due to the loss of sensitivity to the highest spatial frequencies of the DM. Moreover, working in high flux conditions, we consider that measurement noise error is negligible. Hence, we hypothesize that the difference in performance is mainly due to the ground layer sensing (see Fig. 2), spatial aliasing, and tomographic error. In particular, for the tomographic error, super-resolution is valid only where the LGS beams are super-imposed, and it has a lower efficiency where the overlap of the beams is partial. Note that super-resolution is completely useless where the turbulence is sensed by single beams. So, the super-resolution is typically less effective on the external part of the meta-pupil at the highest altitudes, where, as can be seen in Fig. 5, the beams are not super-imposed.

The results for the HARMONI case are shown in Fig. 6. Here, all the turbulence is located at ground level (0 m) as well as the DM, so we can focus only on the the GSR. In fact, the system does not benefit from naturally induced super-resolution in such configuration (therefore these results are also valid for MAORY). The residual phase of the classical approach increases with a slope equal to  $(d/r_0)^{5/6}$  ( $d$  is the SA size) in a similar fashion as the fitting error in an SCAO system. Instead, when super-resolution is introduced, following the features listed above in this section, the slope decreases until it becomes almost flat in the range 100 to 60 SAs ( $d = 0.400 - 0.667$  m).

## 4 LGS Sampling versus Spot Truncation

### 4.1 LGS Spot Size and Sampling

The sampling impacts both the LGSWFS linearity and noise propagation. For the former, as soon as one considers a sampling lower than Shannon (2 pixels per FWHM), an optical gain will appear. For the LGS, this optical gain [conversion between center of gravity (CoG) in pixel, and CoG in arc sec] will be different for  $X$  and  $Y$ , and different for each subapertures. This gain changes with seeing, and monitoring it requires complex calibration procedures. The extreme example is WFSs working with quadcells, and it has been shown that in this case it could represent an important performance limiting factor (e.g., GeMS). But Shannon sampling may become very expensive in terms of pixels required by the LGWFS, and undersampling the LGS spots may be required. The impact of LGS spot undersampling on the centroiding performance has been studied in previous papers (Gratadour et al.,<sup>33</sup> Nicolle et al.,<sup>34</sup> and Ke,<sup>35</sup> Pedreros et al. this review) and is not detailed here. The conclusion (coherent between all the papers) is that one can go down to 1 pixel per FWHM while keeping the final error to a reasonable level.

### 4.2 LGS Spot Truncation

The second big problem when dealing with LGS for an ELT comes from the spot elongation. Spot elongation per se may not be a problem, as long as enough photons are available to perform



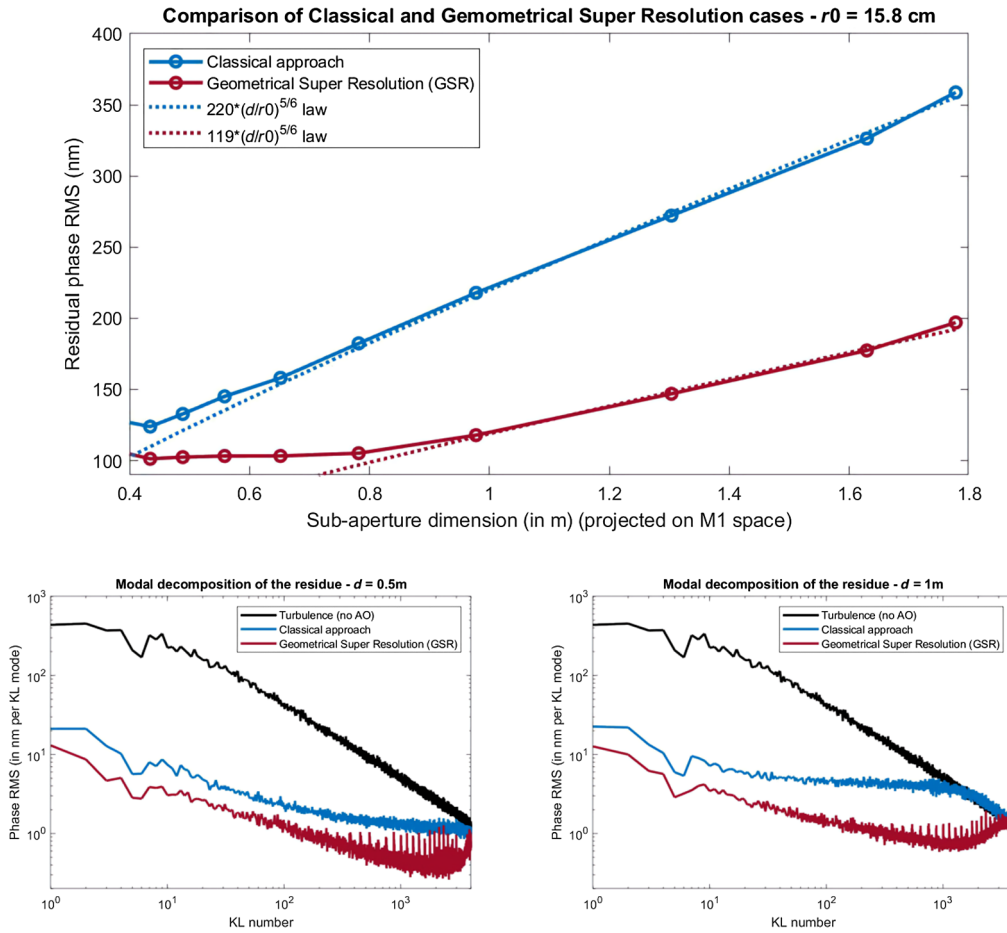


**Fig. 6** Impact on performance of SA size. Note that all the turbulence is located at ground level (0 m) as well as the DM (so no natural induced super-resolution is present). Top: residual phase RMS as a function of the SA dimension. Bottom: turbulence and residual variance modal decomposition on a Karhunen–Loève base for different configurations for 0.5 m (80 SAs in the diameter) and 1 m (40 SAs in the diameter) for each plot, respectively, blue line stands for classical AO, red line stands for GSR, and black line stands for the full turbulent (no AO) case.

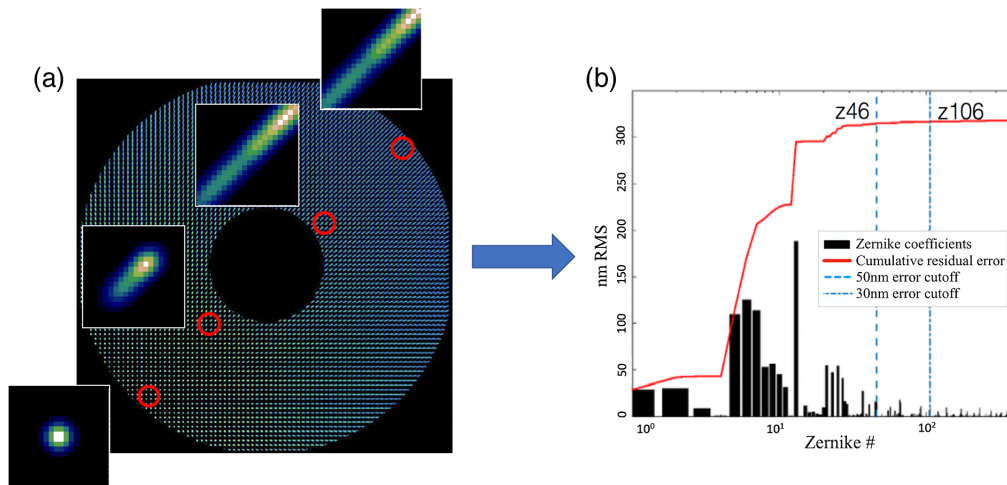


**Fig. 7** Example of spot truncation in the extreme case of a very extended Na profile and a small ( $10'' \times 10''$ ) FoV WFS. (a) One WFS image and (b) the aberrations produced by the spot truncation on the six LGS after propagation through the tomographic reconstructor.

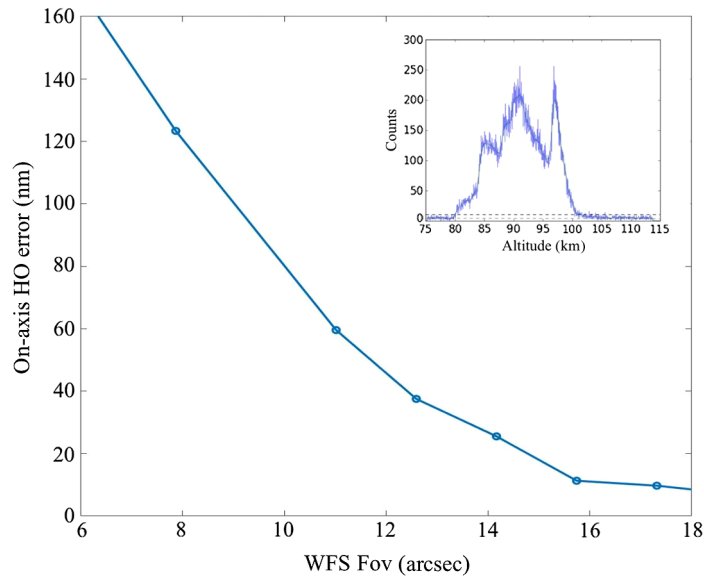


**Fig. 8** On-axis high order (excluding tilts) differential (with respect to a FoV of 22 arc sec) residual as a function of WFS FoV.  $68 \times 68$  SAs very-wide Na profile.<sup>37</sup> Na profile structure is given at Zenith, the simulation have been made for a 30-deg zenith angle with the according stretch of the profile altitude. For this particular profile, the width is estimated to 22 km (this gives on the WFS spots with long axis FWHM up to  $25''$ ). Note that this error is field dependent, but the on-axis trend is representative of the overall error in the corrected FoV.

centroiding. The main issue comes from spot truncation, as this introduces biases in the tomographic reconstruction. Biases may be evolving quickly, at a rate following the Na layer spatial evolution. So truncation and associated biases should be minimized as much as possible. This is made possible by (i) maximising the FoV per SA and (ii) using a regularized reconstruction.

Of course these aberrations are statics for a given profile but Na profiles can evolve quite rapidly (with timescale of a few seconds typically); more importantly, when mixed with turbulence, these effects are randomized and become quite difficult to handle with a dedicated truth sensor. The best solutions from a system point of view are therefore twofold:

1. To increase the Shack–Hartmann SA FoV to reduce the truncation effect at its root.
2. Add a numerical over-regularisation process<sup>8,36</sup> to over-penalize the signal coming from the most truncated in the reconstruction process

We have evaluated the impact of the SA FoV and spot truncation on performance in Fig. 8. As can be seen from Fig. 8, the truncation error can become very significant when the FoV decreases down to 10 arc sec. A reasonable FoV per SA would be to accommodate at least 15 to 16 arc sec.

## 5 Noise Propagation

The last parameter that must be taken into account for the design of the LGSWFSs for the ELT is the sensitivity to noise, both photon and detector noises. We recall that for classical AO system, the final noise contribution :  $\sigma_{\text{noise}}^2$  can be approximated by the following equation:<sup>38</sup>

$$\sigma_{\text{noise},i}^2 = \sigma_{\text{WFS},\lambda_{\text{wfs}}}^2 \left( \frac{\lambda_{\text{wfs}}}{\lambda_{im}} \right)^2 * P_{\text{rec},i} * T_{\text{filtering}} \text{ [in rad}^2 \text{ at } \lambda_{\text{wfs}}\text{]}. \quad (3)$$

And the propagated noise as

$$\sigma_{\text{noise,prop}}^2 = \sum_{i=1}^{n_{\text{corr}}} \sigma_{\text{noise},i}^2 \text{ [in rad}^2 \text{ at } \lambda_{\text{wfs}}\text{]}, \quad (4)$$

where  $\sigma_{\text{WFS},\lambda_{\text{wfs}}}^2$  is the variance of the noise at the WFS level,  $\lambda_{\text{wfs}}$  is the WFSensing wavelength,  $\lambda_{\text{im}}$  is the imaging wavelength,  $P_{\text{rec},i}$  is the coefficient that takes into account the propagation of noise in the phase reconstruction process and  $T_{\text{filtering}}$  is the coefficient that takes into account the propagation of noise in the temporal filtering process. If we assume that statistically all the WFS SAs have the same noise propagation, then we can write:

$$\sigma_{\text{noise,prop}}^2 = \sigma_{\text{WFS},\lambda_{\text{wfs}}}^2 * \left(\frac{\lambda_{\text{wfs}}}{\lambda_{\text{im}}}\right)^2 * T_{\text{filtering}} \sum_{i=1}^{n_{\text{corr}}} P_{\text{rec},i} \text{ [in rad}^2 \text{ at } \lambda_{\text{wfs}}\text{]}. \quad (5)$$

$T_{\text{filtering}}$  mainly depend on the temporal aspect of the AO loop: integration time, read-out time, control law characteristics and loop delay. For a basic (and yet widely used) integrator-like scheme,<sup>38</sup> assuming a two frames delay and a loop gain of 0.5 gives  $T_{\text{filtering}} = 1/10$ .

The main differences between Laser tomographic and classical AO are the following:

1.  $\sigma_{\text{WFS},\lambda_{\text{wfs}}}^2$  is no more the same for all the SA and will depend on the spot elongation.
2.  $P_{\text{rec},i}$  will include a tomographic reconstruction and will differ from a classical modal basis noise propagation matrix, as described in Ref. 12 for example.

An interesting case to study here is the following: an  $N_{\text{lgs}}$  LGS system, without elongation, associated to a tomographic case where all the turbulence will be located in the telescope pupil. In that particular case,  $P_{\text{recLTAO},i} = \frac{1}{N_{\text{lgs}}} P_{\text{rec,SCAO},i}$  and  $\sigma_{\text{WFS},\lambda_{\text{wfs}}}^2$  is the same for all the SAs of all the LGS. The tomographic noise propagation is therefore nothing but  $\frac{1}{N_{\text{lgs}}}$  the SCAO noise propagation.

This extreme case allows us to draw the ultimate limits in terms of performance for any WFS configurations. It will also help to understand the influence of the critical parameters of the WFS design to be adjusted in final design choice.

Let us first study the impact of the main WFS parameters in the ultimate case of photon noise limited detector. For that we study the influence of two main parameters: the spot FWHM (mainly produced by the combination of the spatial extension of the Laser and its propagation through the atmosphere) and the pixel size (projected on sky).

For the photon noise limited case, considering a simple COG, the analytical expression of  $\sigma_{\text{WFS},\lambda_{\text{wfs}}}^2$  can be derived from the standard expressions,<sup>34,39</sup> and expressed as follows:

$$\sigma_{\text{ph},\lambda_{\text{wfs}}}^2 = \frac{\pi^2}{2 \ln(2)} \frac{1}{N_{\text{ph}}} \left( \frac{\sqrt{\text{FWHM}_{\text{spot}}^2 + \text{FWHM}_{\text{pixel}}^2}}{\text{FWHM}_{\text{diff}}} \right)^2 \text{ [in rad}^2 \text{ at } \lambda_{\text{wfs}}\text{]}. \quad (6)$$

where  $\text{FWHM}_{\text{diff}}^2$  is the diffraction limited size of the SA,  $\text{FWHM}_{\text{spot}}$  the FWHM of the spot size in the SA focal plane and  $\text{FWHM}_{\text{pixel}}$  the pixel response. Note that for this last one we have assumed that the pixel FWHM is equal to the physical size of the pixel projected on the sky. This is not always the case but it remains a fairly good approximation for classical detectors used in AO. More importantly, the previous equation is highlighting two fundamental points for an SH:

1. The pixel size of the WFS has to be smaller than the spot size to have a negligible impact on the noise propagation.
2. We can define a number of useful photon  $N_{\text{usefull}}$  as

$$N_{\text{usefull}} = N_{\text{ph}} \left( \frac{\text{FWHM}_{\text{diff}}}{\sqrt{\text{FWHM}_{\text{spot}}^2 + \text{FWHM}_{\text{pixel}}^2}} \right)^2, \quad (7)$$

in other words, enlarging the spot or working with large pixel is equivalent to reducing the WFS efficiency. As an example, working with 1 arcsec pixel combined with 1" FWHM spot is 2.25 times more efficient (in terms of noise variance) than a 1.5" pixel and 1.5" FWHM spot.

In the case of uniform Gaussian noise induced by the detector read out (a.k.a. RON), the number of pixels becomes a critical parameter. Again, considering a classical CoG, the analytical expression of the measurement variance is

$$\sigma_{\text{ron},\lambda_{\text{wfs}}}^2 = \frac{\pi^2}{3} \left( \frac{\text{FWHM}_{\text{pixel}}}{\text{FWHM}_{\text{diff}}} \right)^2 \left( \frac{\text{ron}}{N_{\text{ph}}} \right)^2 \left( \frac{N_s}{N_d} \right)^2 \quad [\text{in rad}^2 \text{ at } \lambda_{\text{wfs}}], \quad (8)$$

where  $\frac{\text{FWHM}_{\text{pixel}}}{\text{FWHM}_{\text{diff}}}$  converts pixel error in radian, ron stands for the read-out noise,  $N_s$  stands for the total number of pixel involved in the CoG computation, and  $N_d$  is the number of pixel in the spot FWHM. Assuming that  $N_s$  is computed as the ratio of a spot area equal to 2 times the spot FWHM and the pixel size, then  $\frac{N_s}{N_d} = 4 * \frac{\text{FWHM}_{\text{spot}}}{\text{FWHM}_{\text{pixel}}}$  as soon as  $\text{FWHM}_{\text{pixel}} < \text{FWHM}_{\text{spot}}$  and  $\frac{N_s}{N_d} = 4$  otherwise.

$$\sigma_{\text{ron},\lambda_{\text{wfs}}}^2 = \frac{\pi^2}{3} \left( \frac{\text{FWHM}_{\text{pixel}}}{\text{FWHM}_{\text{diff}}} \right)^2 \left( \frac{\text{ron}}{N_{\text{ph}}} \right)^2 \left( 4 * \frac{\text{FWHM}_{\text{spot}}}{\text{FWHM}_{\text{pixel}}} \right)^2 \quad [\text{in rad}^2 \text{ at } \lambda_{\text{wfs}}]. \quad (9)$$

And finally the ron contribution to WFS measurement variance can be approximated as

$$\sigma_{\text{ron},\lambda_{\text{wfs}}}^2 = \frac{16\pi^2}{3} \left( \frac{\text{ron}}{N_{\text{ph}}} \right)^2 \left( \frac{\text{FWHM}_{\text{spot}}}{\text{FWHM}_{\text{diff}}} \right)^2 \quad \text{if } \text{FWHM}_{\text{spot}} > \text{FWHM}_{\text{pixel}}, \quad (10)$$

$$= \frac{16\pi^2}{3} \left( \frac{\text{ron}}{N_{\text{ph}}} \right)^2 \left( \frac{\text{FWHM}_{\text{pixel}}}{\text{FWHM}_{\text{diff}}} \right)^2 \quad \text{if } \text{FWHM}_{\text{spot}} < \text{FWHM}_{\text{pixel}}. \quad (11)$$

Here again, it is very easy to understand the importance of the spot FWHM and of the pixel size in the noise produced by any SH measurement. It is essential to minimize these two parameters to have the smallest possible noise and keep the pixel size close (but slightly smaller) than the spot FWHM.

Although it is quite easy to develop analytical formulae under the hypothesis of a single WFS and symmetric and identical (statistically speaking) spot shape for all the SA, in the case of a tomographic AO system none of these hypotheses remains true. If the tendencies highlighted by the theoretical developments remain correct, it is important to have a full simulation to have a better understanding of the limitations and behaviour in a full LTAO or MCAO case. Using full end-to-end simulation but looking at the noise propagation term only, we have estimated the performance sensitivity to photon and RON noise. This is shown by Fig. 9.

Several conclusions can be derived from this figure:

1. For ELT applications and scaling flux returns measured after more than four years of LGS operation at Paranal with adaptive optics facility (AOF), the noise error terms for extended spot (we have considered here some extreme case of Na profile) remains quite reasonable: around 50-nm rms.
2. The very first increase of noise from blue to green line is due to the spot elongation. For photon noise only, going from a point link source to an extended LGS increases the noise from 15- to 41-nm rms, which is a quadratic increase of 38-nm rms.
3. The pixel size [as shown in Eq. (6)] is also an important parameter. In the photon limited case, its increase by a factor 4 (from 0.42 to 1.68") has led to an additional noise error of 40-nm rms (quadratic increase). In other words, a factor 4 of sampling increase has the same impact on noise propagation than the spot elongation itself.
4. Note that for the specific case of a pixelscale of 1.68", non-linearities (pixel scale larger than spot FWHM) should have started to degrade the performance. These non-linearities are not properly modeled in the simulations, and these results are then optimistic. For a real system to work with such a large pixel scale, on-line gain tracking would be required (see Sec. 2.3).
5. Adding RON has a dramatic impact for low flux cases. In the typical range of return flux we will have to consider with the ELT and considering RON smaller than  $3e-$ , the impact

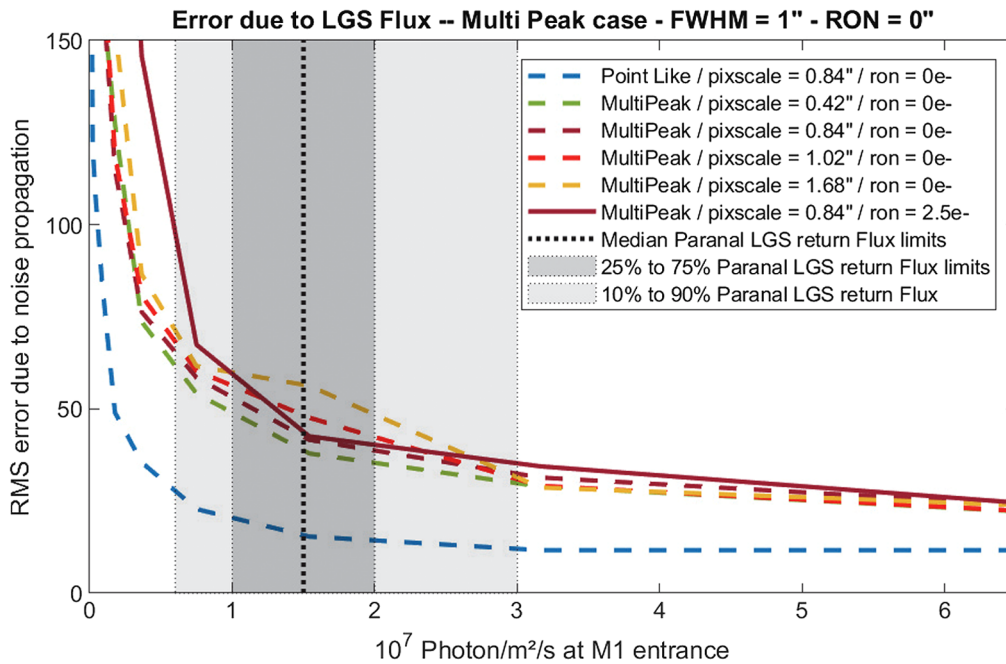


**Fig. 9** Impact of Na return flux on performance. Error RMS as a function of the Na return flux for point like and multi-peak<sup>37</sup> Na profile, different pixel scales and  $68 \times 68$  SAs.

remains very small. Note that we have considered here a very basic  $3\sigma$  threshold algorithm for the centroiding measurements. A more clever approach (weighted CoG, correlation or match filter) will further reduced the impact.

In conclusion, with an end-to-end simulation and looking at the noise propagation error term only, we have shown that noise propagation error remains quite low for a LTAO or a MCAO system working with Paranal typical flux return. The RON is not an major contributor for the level considered here ( $2.5 e^-$ ). Pixel scales have to remain reasonably small with a good (not to say optimal) compromise around the typical size of the spot small axis FWHM (that is around  $1''$ ).

## 6 Potential LGSWFS Designs

In the previous sections we have derived the performance sensitivity to several factors, like the pupil spatial sampling, LGS spot sampling and impact of truncation. In this section, we have now to put these sensitivity analyses in front of expected LGS parameters and eventually provide recommendations on what a LGSWFS could be for the ELT. This should not be seen as a design definition, but guidelines for tomographic AO systems for the ELT. Of course, LGSWFS design choices strongly depends on the Na characteristics, so we begin this section by an overview of typical Na parameter distribution derived from the VLT operation.

### 6.1 Sodium Typical Characteristics

The AOF<sup>40</sup> has been operational on the UT4 telescope at Paranal since 2017, providing access to a deformable secondary mirror and four LGS units (4LGSF) for a variety of instruments. The GALACSI AO module is also part of the modules delivered within the AOF, bringing AO correction capabilities for the multi unit spectroscopic explorer instrument, and is also a great tool to gather statistics on the Na layer characteristics thanks to the continuous logging of the AO telemetry data.

The LGS spot size on the sky is dependent on the seeing but also on the LLT design. The on-sky spots measured during the 4LGSF commissioning phase had an FWHM of  $1.05''$  for the

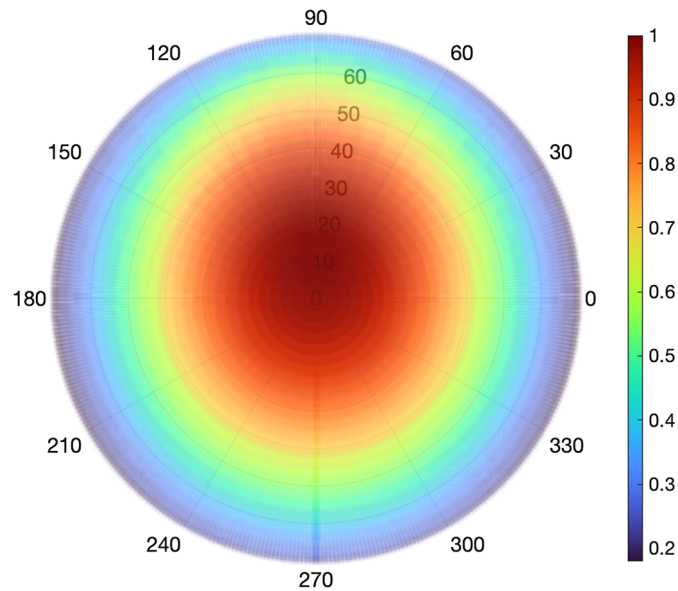


**Fig. 10** Sky plot of the theoretical LGS flux return at Paranal for a seeing of  $0.8''$ , normalized to the maximum value, based on the LGSBloch model ( $N = 90$ ,  $E = 0$ ). The variations are mostly dependent, in addition to the pointing direction, on the local direction and magnitude of the geomagnetic field, and on the laser power, polarization state, and re-pumping efficiency.

small axis and  $1.61''$  for the long axis, with the atmosphere seeing being  $0.6''$  and UT4 pointing altitude of  $60$  deg. The difference between the small and long axes comes from the spot elongation, due to the extended structure of the Na layer, the position of the launch telescope on the side of the pupil, and the distance between the launch telescope and the position in the pupil where it is measured. On-sky measurements were also performed at different pointing altitudes showing no significant dependence and with different seeing conditions. With a seeing of  $1''$ , the on-sky measured spot size was about  $1.35''$  for the small axis and  $2.1''$  for the long axis. These spot sizes were measured on the UT4 guiding camera for the full 8-m aperture and with the LGS in the center of the field. The launch telescopes for the LGS on the ELT will be identical to the ones of the VLT, and the spot size validated on-sky can thus be used for ELT AO simulations.

During on-sky operation of GALACSI, the fluxes of all four WFSs are logged regularly. Data are available since July 2017 and are processed to derive the statistics of returned flux, converted to photons per second and per  $m^2$  at M1 entrance. The first parameter impacting the flux return is the pointing direction of the telescope at the time of the observation.<sup>41</sup> Figure 10 presents the sky plot of the simulated LGS flux return for a seeing of  $0.8''$ , a sodium abundance of  $4 \times 10^{13}$  atoms/ $m^2$ , and a 20-W class laser at Paranal, showing the high variability of the return flux versus the pointing direction.

The second parameter affecting the LGS flux return is the Na column abundance, which varies with time, on both long- and short-time scales. The Na column abundance in atoms/ $m^2$  can be retrieved from the return flux measured on GALACSI, by correcting for the effect of the pointing direction. Figure 11 shows the statistics of the Na column abundance per month. The violin representation shows the distribution of the Na column abundance from all the measurements of each month. The median value is shown as a red dot. The months when too few measurements were obtained to be statistically relevant have been marked with a 0. The known seasonal cyclic variation between the summer (low return) and winter (high return) months can be seen on the measurements. Differences can also be seen from year to year in the global average. Atmosphere studies show that the Na abundance is correlated to the Sun activity cycle of 11 years.<sup>42</sup> The last peak of the Sun activity was in 2014, with a decrease since that date. The prediction for the Sun activity shows a minimum in 2021 and the start of a new cycle with the next peak in 2025.

The morphology and temporal variations of the Na layer has been studied with different methods and at different sites.<sup>37,43,44</sup> No measurements (morphology and/or temporal) of this

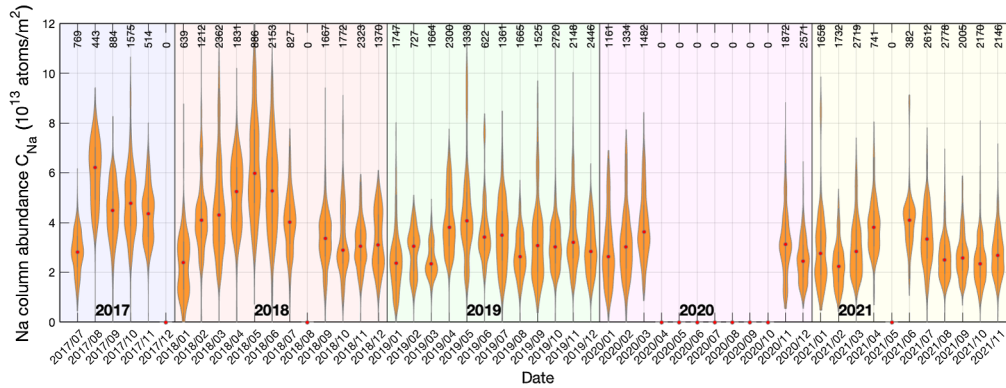


Fig. 11 Statistics of Na column abundance per month.

type exist for the VLT or ELT, but the three studies reported similar results for a very different location on Earth and their results can thus be considered representative for the ELT also. The following parameters can thus be used to describe the general structure of the Na layer, with all altitude given above sea level: mean centroid altitude of  $90.8 \pm 0.1$  km, altitude range (containing 95% of the photons) of  $13.1 \pm 0.3$  km (minimum width of 6 km a maximum one of 21 km), mean lower edge altitude of  $81.7 \pm 0.1$  km, mean upper edge altitude of  $104.9 \pm 0.3$  km.

The mean altitude also shows variations during the course of a night. The power spectral density of these variations can be represented by a power law:  $P_a(\nu) = \alpha\nu^\beta$ , with  $\nu$  the fluctuations frequency. The amplitude  $\alpha$  and power coefficient  $\beta$  show variations from night to night, but can be represented by the following mean values:  $\alpha = 34.4_{-4.8}^{+5.6}$   $\text{m}^2 \text{Hz}^{-1}$  and  $\beta = -1.87 \pm 0.02$ .

The Na density vertical structure is also showing a high variability, and it is considered difficult to define any kind of typical vertical profile. An attempt has still been made at classifying the zoo of profiles measured on-sky into seven different classes.<sup>37</sup>

## 6.2 Toward LGSWFS for the ELT

In this section, and based on the Na inputs derived above, we evaluate the boundary conditions recommended for the main LGSWFS parameters for the ELT, which are the number of SAs (pupil sampling), the FoV per SA, and the pixel scale. The intention here is not to explore all the potential combinations of these parameters, but rather to provide what we think are boundary conditions to provide a LGSWFS design that would be robust to changing conditions. There may be ways to push each of these boundaries by implementing custom hardware or smart software solutions, and we are not claiming that the proposed boundaries are hard limits. We only highlight one potential implementation that we know will be working. Of course, hidden behind this

Table 1 LGSWFS main parameters for an ELT (40 m) telescope.

Parameters	Range	Comments
Subaps	$>64^2$	See Fig. 6. Use of super resolution allows use of less subapertures than DM actuators, but the larger the sampling, the better the performance. Going down to $64 \times 64$ has negligible impact on the performance.
FOV	$>16^2$ arc sec <sup>2</sup>	See Fig. 8. The larger the FoV, the better the performance. Going above 16 arcsec allows minimizing the truncation error for the worst Na profiles
Pixel scale	$<1.15$ arc sec	This is set by the minimum expected LGS spot size, and to maintain a good sampling and a decent noise propagation (see Fig. 9).
RON	$<3 e^-$	With a good target around $2.5 e^-$ . This value is fixed to be almost photon noise limited in the typical range of LGS flux return (see Fig. 9)

trade-off are the detectors characteristics, which are the number of pixels, the frame rate, and the RON. Depending on the detector availability and performance, one can adjust the LGSWFS parameters to fit into a given detector format, and the sensitivity study presented here allows that. Here, we have provided boundaries for the LGSWFS parameters, which allows one to optimize the performance, assuming that suitable detectors are available (e.g., Ke, Pedreros et al. this review). These trade-offs are summarized in Table 1. Basically, based on the trade-off between pupil sampling, LGS spot truncation and LGS spot sampling, the recommendation for the ELT would be to deploy LGSWFSs with  $>64 \times 64$  subapertures,  $>16''$  FoV and a pixel scale  $<1.15''$ . The overall error budget would increase if the parameters of the LGSWFSs deviate from the ones indicated above and if no specific hardware or software solutions are implemented. Note that a practical implementation based on these numbers is described in Ke, Pedreros et al. (this review).

## 7 Conclusion

In this paper, we have explored the key LGSWFS parameters impacting the performance when deployed at the ELT scale. When going from the current generation of 8- to 10-m telescopes to a 40-m scale, the first challenge comes from the LGS spot elongation. Where it only represents a few arcseconds for 8- to 10-m telescope, it becomes a major limitation for ELT, with expected elongations of up to 25 arc sec. Designing an LGSWFS then becomes a challenge, as one has to manage both the FoV and the small axis sampling. As this is out of reach of current detector technologies, a trade-off has to be made. In this paper, we open a new dimension in this trade-off, but making use of super resolution, and by taking advantage of the fact that we have several LGSWFS looking at an almost similar turbulence volume. Combining the signal from the multiple WFSs, we show that we can go beyond the historical paradigm of matching the subapertures count with the DM actuators geometry. Due to super resolution, we show that fewer subapertures per WFS can be used, which opens the path for LGSWFS design based on existing or realistic detector hardware.

## Acknowledgments

This work benefited from the support the following grants: WOLF ANR-18-CE31-0018, F-CELT ANR-21-ESRE-0008 and LabEx FOCUS ANR-11-LABX-0013 of the French National Research Agency (ANR), OPTICON H2020 (2017–2020) Work Package 1 (Calibration and test tools for AO assisted E-ELT instruments) under grant No. 730890, Action Spécifique Haute Résolution Angulaire (ASHRA) of CNRS/INSU co-funded by CNES.

## References

1. R. Tamai et al., “The ESO’s ELT construction progress,” *Proc. SPIE* **11445**, 114451E (2020).
2. E. Vernet et al., “ELT M4—the largest adaptive mirror ever built,” *Messenger* **178**, 3–4 (2019).
3. R. Ragazzoni, “Pupil plane wavefront sensing with an oscillating prism,” *J. Mod. Opt.* **43**, 289–293 (1996).
4. R. Ragazzoni et al., “Extending the pyramid WFS to LGSs: the INGOT WFS,” *Proc. SPIE* **10703**, 107033Y (2018).
5. S. Esposito et al., “Pyramid wavefront sensing using laser guide star for 8m and ELT class telescopes,” *Proc. SPIE* **9909**, 99096B (2016).
6. C. Arcidiacono et al., “Ingot wavefront sensor: from the Fourier End2End numerical simulation to the LOOPS test bench,” *Proc. SPIE* **11448**, 1144868 (2020).
7. E. Gendron, “Optical solutions for accommodating ELT LGS wave-front sensing to small format detectors,” *Proc. SPIE* **9909**, 99095Z (2016).
8. S. Oberti et al., “LGS tomography and spot truncation: tips and tricks,” in *6th Int. Conf. Adapt. Opt. for Extremely Large Telesc.*, Québec, Canada (2019).



9. L. Bardou et al., “ELT-scale elongated LGS wavefront sensing: on-sky results,” *Astron. Astrophys.* **649**, A158 (2021).
10. P. Ciliegi et al., “MAORY: the adaptive optics module for the Extremely Large Telescope (ELT),” *Proc. SPIE* **11448**, 114480Y (2020).
11. N. A. Thatte et al., “HARMONI: first light spectroscopy for the ELT: instrument final design and quantitative performance predictions,” *Proc. SPIE* **11447**, 114471W (2020).
12. F. Rigaut and E. Gendron, “Laser guide star in adaptive optics: the tilt determination problem,” *Astron. Astrophys.* **261**, 677–684 (1992).
13. J.-M. Conan, G. Rousset, and P.-Y. Madec, “Wave-front temporal spectra in high-resolution imaging through turbulence,” *J. Opt. Soc. Am. A* **12**, 1559–1570 (1995).
14. C. Plantet et al., “Sky coverage assessment for the European ELT: a joint evaluation for MAORY/MICADO and HARMONI,” *J. Astron. Telesc. Instrum. Syst.* **8**(2), 021509 (2022).
15. D. L. Fried and J. F. Belsher, “Analysis of fundamental limits to artificial-guide-star adaptive-optics-system performance for astronomical imaging,” *J. Opt. Soc. Am. A* **11**, 277–287 (1994).
16. E. N. Ribak and R. Ragazzoni, “Reduction of laser spot elongation in adaptive optics,” *Opt. Lett.* **29**, 1351–1353 (2004).
17. W. Jahn et al., “Laser guide star spot shrinkage for affordable wavefront sensors,” *Proc. SPIE* **9909**, 99096L (2016).
18. L. Gilles and B. Ellerbroek, “Shack–Hartmann wavefront sensing with elongated sodium laser beacons: centroiding versus matched filtering,” *Appl. Opt.* **45**, 6568–6576 (2006).
19. C. Béchet et al., “Closed-loop ground layer adaptive optics simulations with elongated spots: impact of modeling noise correlations,” in *Adapt. Opt. for Extremely Large Telesc.*, p. 03004 (2010).
20. D. Gratadour, E. Gendron, and G. Rousset, “Intrinsic limitations of Shack–Hartmann wavefront sensing on an extended laser guide source,” *J. Opt. Soc. Am. A* **27**, A171 (2010).
21. S. J. Thomas et al., “Study of optimal wavefront sensing with elongated laser guide stars,” *Mon. Not. R. Astron. Soc.* **387**, 173–187 (2008).
22. J. G. Robertson, “Detector sampling of optical/IR spectra: how many pixels per FWHM?” *Publ. Astron. Soc. Australia* **34**, e035 (2017).
23. J.-P. Véran and G. Herriot, “Centroid gain compensation in Shack–Hartmann adaptive optics systems with natural or laser guide star,” *J. Opt. Soc. Am. A* **17**, 1430–1439 (2000).
24. M. A. van Dam, “Measuring the centroid gain of a Shack–Hartmann quad-cell wavefront sensor by using slope discrepancy,” *J. Opt. Soc. Am. A* **22**, 1509–1514 (2005).
25. B. Neichel et al., “Gemini multiconjugate adaptive optics system review—II. Commissioning, operation and overall performance,” *Mon. Not. R. Astron. Soc.* **440**, 1002–1019 (2014).
26. J. M. Beckers, “Adaptive optics for astronomy: principles, performance, and applications,” *Annu. Rev. Astron. Astrophys.* **31**, 13–62 (1993).
27. M. Sarazin et al., “Defining reference turbulence profiles for E-ELT AO performance simulations,” in *Proc. 3rd AO4ELT Conf.*, S. Esposito and L. Fini, Eds., p. 89 (2013).
28. L. Busoni et al., “Adaptive optics design status of MAORY, the MCAO system of European ELT,” in *6th Int. Conf. Adapt. Opt. for Extremely Large Telesc.*, Québec, Canada (2019).
29. S. Oberti et al., “MAORY design trade-off study: tomography dimensioning,” in *Adapt. Opt. for Extremely Large Telesc.* (2017).
30. S. Oberti et al., “Super-resolution wavefront reconstruction,” *Astron. Astrophys.* Submitted.
31. B. L. Ellerbroek and F. Rigaut, “Methods for correcting tilt anisoplanatism in laser-guide-star-based multiconjugate adaptive optics,” *J. Opt. Soc. Am. A* **18**, 2539–2547 (2001).
32. L. Wang, D. Andersen, and B. Ellerbroek, “Sky coverage modeling for the whole sky for laser guide star multiconjugate adaptive optics,” *Appl. Opt.* **51**, 3692 (2012).
33. D. Gratadour et al., “Comparing centroiding methods for Shack-Hartmann wavefront sensing with laser guide stars on an ELT,” *Proc. SPIE* **7736**, 77361A (2010).
34. M. Nicolle et al., “Improvement of Shack-Hartmann wave-front sensor measurement for extreme adaptive optics,” *Opt. Lett.* **29**, 2743–2745 (2004).

35. Z. Ke et al., “Performance of a complementary metal-oxide-semiconductor sensor for laser guide star wavefront sensing,” *J. Astron. Telesc. Instrum. Syst.* **8**(2), 021511 (2022).
36. T. Fusco et al., “A story of errors and bias: the optimization of the LGS WFS for HARMONI,” in *AO4ELT6*, Quebec City, Canada (2019).
37. T. Pfrommer and P. Hickson, “High resolution mesospheric sodium properties for adaptive optics applications,” *Astron. Astrophys.* **565**, A102 (2014).
38. F. Roddier, Ed., *Adaptive Optics in Astronomy*, Cambridge University Press, Cambridge; New York (1999).
39. G. Rousset, *Wave-Front Sensors in Adaptive Optics in Astronomy*, Cambridge University (1999).
40. R. Arsenault et al., “Progress on the VLT adaptive optics facility,” *Messenger* **142**, 12–16 (2010).
41. R. Holzlohner et al., “Laser guide star return flux simulations based on observed sodium density profiles,” *Proc. SPIE* **7736**, 77360V (2010).
42. D. M. Simonich, B. R. Clemesha, and V. W. J. H. Kirchhoff, “The mesospheric sodium layer at 23S: nocturnal and seasonal variations,” *J. Geophys. Res.* **84**, 1543–1550 (1979).
43. J. Castro-Almazan et al., “Na LGS height profiles at Teide Observatory, Canary Islands,” in *5th Int. Conf. Adapt. Opt. for Extremely Large Telesc.*, Tenerife, Canary Islands, Spain (2017).
44. B. Neichel et al., “Characterization of the sodium layer at cerro pachon, and impact on laser guide star performance,” *Mon. Not. R. Astron. Soc.* **429**, 3522–3532 (2013).

**Thierry Fusco** is the science deputy director of the ONERA Optics Department. He has 25 years of expertise in adaptive optics and post-processing for astronomy. After his PhD in 2000 on the mitigation of partial correction and anisoplanatism in AO, he was the VLT-SPHERE AO scientist (extreme AO system for direct detection and characterization of extrasolar planet) from 2004 to 2015 and he is now the AO scientist of HARMONI (which gathers both a classical and laser tomographic AO system) the first light integral field spectrograph instrument for the European ELT.

**Guido Agapito** is a researcher at INAF, Osservatorio Astrofisico di Arcetri, Adaptive Optics Group since 2008. His work focuses on simulation and control of AO systems, and he is involved in the design and commissioning of several instruments, including Multiconjugate Adaptive Optics RelaY (MAORY) for ELT, Enhanced Resolution Imager and Spectrograph (ERIS), and MCAO-Assisted Visible Imager and Spectrograph (MAVIS) for VLT, and Single conjugated adaptive Optics Upgrade for LBT (SOUL).

Biographies of the other authors are not available.